Journal of Hazardous Materials 188 (2011) 212–220

Contents lists available at ScienceDirect

Journal of Hazardous Materials

journal homepage: www.elsevier.com/locate/jhazmat

Preparation and characterization of photoactive composite kaolinite/TiO_2

K. Mamulová Kutláková[a,*], J. Tokarský[a], P. Kovář[b], S. Vojtěšková[a], A. Kovářová[b], B. Smetana[c], J. Kukutschová[a], P. Čapková[a], V. Matějka[a]

[a] Nanotechnology Centre, VŠB-Technical University of Ostrava, 17. listopadu 15/2172, 708 33 Ostrava-Poruba, Czech Republic
[b] The Czech Technological Centre for Inorganic Pigments a.s., Přerov, Czech Republic
[c] Department of Physical Chemistry and the Theory of Technological Processes, VŠB-Technical University of Ostrava, 17. listopadu 15/2172, 708 33 Ostrava-Poruba, Czech Republic

ARTICLE INFO

Article history:
Received 1 October 2010
Received in revised form 4 January 2011
Accepted 25 January 2011
Available online 1 February 2011

Keywords:
Kaolin
TiO_2
Composite
Photoactivity

ABSTRACT

Preparation of nanocomposite kaolinite/TiO_2, using hydrolysis of titanyl sulfate in the presence of kaolin was addressed. A variable (kaolin)/(titanyl sulfate) ratio has been used in order to achieve the desired TiO_2 content in prepared nanocomposites. Calcination of the composites at 600 °C led to the transformation of the kaolinite to metakaolinite and to origination of metakaolinite/TiO_2 composites. The prepared samples were investigated using X-ray fluorescence spectroscopy, X-ray powder diffraction, Fourier transform infrared spectroscopy, scanning electron microscopy, thermogravimetry and diffuse reflectance spectroscopy in the UV–VIS region. Structural ordering of TiO_2 on the kaolinite particle surface was modeled using empirical force field atomistic simulations in the *Material Studio* modeling environment. Photodegradation activity of the composites prepared was evaluated by the discoloration of Acid Orange 7 aqueous solution.

1. Introduction

Nanosized titanium dioxide (TiO_2) is the most frequently studied photocatalyst currently. The surface and structural properties of TiO_2 were summarized in detail by Diebold [1]. Titanium dioxide may occur in three modifications according to ambient conditions – anatase, brookite and rutile. Among these modifications, the anatase form is a material with promising properties due to its high photocatalytic activity. The principle of the photodegradation mechanism of TiO_2 can be found in the review article published by Carp et al. [2].

Many techniques are utilized for TiO_2 nanoparticles synthesis and the article published by Xiabo and Mao [3] offers their overview. The sol–gel procedure is among the most frequently used methods and the common precursors are titanium(IV) alkoxides, mainly titanium(IV) tetraisopropoxide, and titanium(IV) *n*-butoxide (or titanium(IV) tert-butoxide) [4,5]. In spite of numerous advantages connected with these precursors, the unquestionable fact is that they are too expensive to be employed for preparation of large scale samples. Consequently a large effort has been devoted towards use of low cost intermediates: mainly titanylsulfate ($TiOSO_4$) [6] and titanium tetrachloride ($TiCl_4$) [7], which are obtained during the sulfate or the chloride procedure of TiO_2 white-pigment manufacturing.

The main application of anatase is in the field of photocatalysis, especially degradation of environmental contaminants. Photodegradation activity of TiO_2 is proven with degradation of model substances presented in liquid as well as in gaseous phase. The anatase may allow for degradation of organic dyes [8], phenol [9], pesticides [10] in liquid phase, e.g., in contaminated waters. In a gaseous phase the degradation of nitric oxides [11], toluene [12] and formaldehyde [13] was observed. Photodegradation test with organic dyes represents an easy and fast estimation of TiO_2 photodegradation activity. The rate of the degradation can be monitored by the change in the absorption of the dye solution by the UV–VIS spectrometry. In the case when TiO_2 forms a finely dispersed suspension in a dye solution, the photocatalyst has to be removed by filtration or ultracentrifugation before a measurement of UV–VIS absorption. The complete separation of TiO_2 is almost impossible if its size is in the order of nanometers. If the TiO_2

Abbreviations: E_{ad}, adhesion energy [kcal]; E_{tot}, total energy of the nanocomposite [kcal]; $E_{tot,KLT}$, total energy of the kaolinite substrate [kcal]; E_{tot,TiO_2}, total energy of the TiO_2 nanoparticle [kcal]; K, kaolin; K6, kaolin calcined at 600 °C; KATI, titanium oxide nanoparticles/kaolinite nanocomposite; KATI12, composite dried at 105 °C and containing 20 wt.% of TiO_2; KATI14, composite dried at 105 °C and containing 40 wt.% of TiO_2; KATI16, composite dried at 105 °C and containing 60 wt.% of TiO_2; KATI62, composite calcined at 600 °C and containing 20 wt.% of TiO_2; KATI64, composite calcined at 600 °C and containing 40 wt.% of TiO_2; KATI66, composite calcined at 600 °C and containing 60 wt.% of TiO_2; KLT, kaolinite; M, muscovite; MKLT, metakaolinite; MS, Accelrys Materials Studio modeling environment; Q, quartz; QEq, charge equilibration method; TiO_2(1), pure TiO_2 powder dried at 105 °C; TiO_2(6), pure TiO_2 powder calcined at 600 °C; UFF, universal force field.

* Corresponding author.
E-mail address: katerina.mamulova.kutlakova@vsb.cz (K. Mamulová Kutláková).

0304-3894/$ – see front matter © 2011 Elsevier B.V. All rights reserved.
doi:10.1016/j.jhazmat.2011.01.106

nanoparticles are fixed on the surface of the suitable particulate substrate, then separation of the photocatalyst can be accomplished easily by filtration or, in the case of bigger carrier particles, by sedimentation.

Despite the fact that TiO_2 is referred as a material with very low toxicity [14,15], there are many studies dealing with possible hazards of TiO_2 nanoparticles [16]. This issue becomes important during entire life cycle of a material containing TiO_2 nanoparticles, which can be potentially released to the environment during manufacturing, usage or disposal. Paints containing nanosized photocatalysts, as well as the polymer/TiO_2 nanocomposites, represent possible danger by the means of releasing of nanosized particles due to the deterioration of material cohesion [17,18]. Growing and anchoring of the nanosized TiO_2 particles on the surface of a suitable substrate prevents the release of nanoparticles to the environment, whereas the substrates can represent an inert part [19], or can bring additional functions at final composite [20,21]. A number of substrates has already been studied for anchoring of the TiO_2 on their surface. Preparation of a TiO_2 thin layer on glass substrates by dip or spin coating is widely investigated [22,23]. The resulting glass shows superhydrophilicity which is reflected in anti-fogging and self-cleaning properties. Silica particles were also studied as a matrix for TiO_2 growth and many authors showed, that the prepared SiO_2/TiO_2 composites have improved photodegradation activity against model pollutants [24,25].

Phyllosilicates are abundant natural materials with a wide scale of practical applications (among others, as sorbents for cations of heavy metals Cd, Zn, Pb, etc. [26]). Due to their unique crystallochemical properties, phyllosilicates represent a suitable matrix for anchoring of TiO_2 nanoparticles [27–29]. Montmorillonite belonging to the 2:1 phyllosilicate group is mentioned more often as a matrix for TiO_2 nanoparticles than other phyllosilicates like vermiculite, kaolinite, saponite, hectorite, etc. In most cases the preparation procedure uses titanium alkoxides as the precursors for clay/TiO_2 composites preparation. Kameshima et al. [30] described preparation of montmorillonite/TiO_2 composite using titanium(IV) tetra iso-propoxide and demonstrated enhanced photodegradation activity of the prepared composite against 1,4-dioxane in comparison to pure photoactive anatase. Machado et al. [31] used exfoliated vermiculite (also belonging to 2:1 group) particles with size in the range of 0.2–0.5 mm and titanium tetraisopropoxide for preparation of the vermiculite/TiO_2 composite. Prepared composite floats on the water surface and shows enhanced photodegradation activity against textile dye Drimaren Red. Kaolinite (1:1 group) as a substrate for nanosized TiO_2 growing was used by Chong et al. [32]. They described a two-step procedure for the KATI composite preparation using titanium(IV) butoxide. Prepared composite showed enhanced photodegradation ability against dye Congo Red.

In this work we focused on the preparation and characterization of the KATI composites using thermal hydrolysis of kaolin and $TiOSO_4$ suspension. Using a simple hydrothermal procedure the composites containing 20 wt.%, 40 wt.% and 60 wt.% of TiO_2 were prepared. Prepared samples were characterized by X-ray powder diffraction method (XRPD), X-ray fluorescence spectroscopy (XRFS), Fourier transform infrared spectroscopy (FTIR) and scanning electron microscopy (SEM). Specific surface area was characterized using the Brunauer–Emmett–Teller (BET) method, thermal properties were studied with thermogravimetric analysis (TG), and UV–VIS diffuse reflectance spectroscopy (UV–VIS DRS) was used for characterization of optical properties of composites prepared. Photoactivity of the prepared composites was evaluated by means of photodegradation of Acid Orange 7 (AO7) model solution. Atomistic simulations using an empirical force field in the *Materials Studio* (*MS*) modeling environment have been carried out in order to study structure and adhesion forces in the KATI composite.

Table 1
Chemical composition of raw K and prepared composites KATI12, KATI14 and KATI16 (in wt.%). LOI, lost on ignition.

Sample	Al_2O_3	SiO_2	SO_3	K_2O	TiO_2	Fe_2O_3	LOI
K	32.4	52.1	<0.00050	1.450	1.15	0.640	10.9
KATI12	21.8	37.4	1.56	1.070	25.8	0.532	12.5
KATI14	15.0	25.6	3.13	0.707	42.5	0.288	14.9
KATI16	9.1	16.1	4.53	0.433	57.2	0.144	16.0

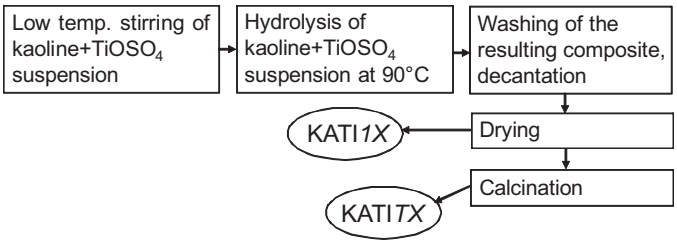

Fig. 1. The scheme of synthesis procedure for composites KATI.

2. Materials and methods

2.1. Sample preparation

Kaolin (K) sample SAK47 (LB MINERALS s.r.o.) was dried for 3 h at 105 °C in order to remove the adsorbed water, and the chemical composition of dried sample K is shown in Table 1. $TiOSO_4$ (PRECHEZA a.s.) containing 102 g of TiO_2 per 1 dm^3 of suspension was used as a TiO_2 precursor. In a typical experiment 50 g of K is mixed with an appropriate volume of $TiOSO_4$ to give the desired amount of TiO_2 in the final composite. The composites are denoted as KATI1*X* or KATI6*X*, where symbol 1 means that the composite was dried at 105 °C, symbol 6 shows the calcination temperature (600 °C for 2 h), symbol *X* denotes the amount of TiO_2 in the final composite (2 for 20 wt.%, 4 for 40 wt.%, 6 for 60 wt.%). The procedure scheme is shown in Fig. 1.

As a reference sample the pure TiO_2 powder was prepared in the same way as presented in Fig. 1 and denoted as TiO_2(1) and TiO_2(6), respectively.

2.2. Characterization methods

2.2.1. X-ray fluorescence

Chemical composition of the prepared samples was determined using energy dispersive fluorescence spectrometer (XRFS) SPECTRO XEPOS (SPECTRO Analytical Instruments GmbH) equipped with 50 W Pd X-ray tube. The samples analyzed were prepared in the form of pressed tablets (wax was used as binder) for this measurement.

2.2.2. Combustion method (determination of sulfur content)

Sulfur content was determined using the CS244 carbon/sulfur analyzer (LECO Corporation) equipped with an induction furnace HT1000. Combustion process was realized in ceramic crucibles filled with 1 g of flux LECOCEL (tungsten particulates) and 1 g of iron chip accelerator.

2.2.3. Scanning electron microscopy

The morphology of composite particles was observed by SEM Philips XL 30 (PHILIPS). Samples were coated with an Au/Pd film and the SEM images were obtained using a secondary electron detector. Elemental composition of samples was determined using energy dispersive X-ray analysis (EDS).

2.2.4. BET analysis

Specific surface area (SSA) of the powder samples was analyzed by nitrogen adsorption in a NOVA 4000e (QUANTACHROME INSTRUMENTS) nitrogen sorption apparatus. The samples were degassed for 3 h at 105 °C before the measurement. SSA was determined by multipoint BET method using the adsorption data in the relative pressure range of 0.1–0.3.

2.2.5. X-ray powder diffraction

The XRPD patterns were recorded under CoKα irradiation (λ = 1.789 Å) using the Bruker D8 Advance diffractometer (Bruker AXS) equipped with a fast position sensitive detector VÅNTEC 1. Measurements were carried out in the reflection mode, powder samples were pressed in a rotational holder. Phase composition was evaluated using database PDF 2 Release 2004 (International Centre for Diffraction Data).

2.2.6. Fourier transformed infrared spectroscopy

Mid FTIR spectra were recorded in the range from 400 to 4000 cm^{-1} for samples in KBr pellet form (1.5 mg of sample in 300 mg of KBr) with a Perkin Elmer 2000 FT-IR spectrometer (Perkin Elmer).

2.2.7. UV–VIS diffuse reflectance spectroscopy

UV–VIS DRS was used for a qualitative description of the differences in the band gap shift depending on the amount of TiO_2 in the studied composites. UV–VIS DR spectra of the powder samples placed in a 5 mm quartz cell were registered using spectrophotometer CINTRA 303 (GBC Scientific Equipment) equipped with a reflectance sphere.

2.2.8. Thermogravimetric analysis

TG was carried out with a SETSYS 18TM thermal analyser (SETARAM Instrumentation) and S-type measuring rod. Samples (13 mg) placed in an alumina crucible were analyzed in an air atmosphere with a heating rate of 10 °C min^{-1} from 25 °C to 1100 °C.

2.2.9. Evaluation of photodegradation activity

Photodegradation activity of the prepared composites was evaluated in a liquid phase, using discoloration of AO7. In order to achieve the adsorption equilibrium in the first part of the experiment, the suspension containing 0.05 g of the photocatalyst, 65 ml of demineralized water and 5 ml of the AO7 aqueous solution ($c_0 = 6.259 \times 10^{-4}$ mol dm^{-3}) was stirred in the dark for 60 min. After 1 h of the adsorption period the suspension was exposed to UV irradiation (UVP pen ray lamp, 365 nm). The extent of AO7 photodegradation was evaluated by the change in the intensity of absorption maximum of AO7 (480 nm) using CINTRA 303 UV-VIS spectrometer.

2.2.10. Molecular modeling

The geometry optimization of KATI nanocomposite models and adhesion energy calculations have been carried out in the *MS* in *Forcite module* using *Universal force field* (UFF). A smart algorithm was used for the geometry optimization with 50,000 iterations. The atom based summation method has been used for the non-bond contributions (Coulombic and van der Waals) to the total potential energy. Charges were calculated using the charge equilibration (QEq) method.

3. Results and discussion

3.1. Chemical and phase composition of the samples

Chemical composition of raw K used for composite preparation and resulting composites KATI12, KATI14 and KATI16 is shown in Table 1. It is evident that increasing TiO_2 content leads to an increase of sulfur content. The increment in loss on ignition (LOI) values for the samples follows the increment of sulfur content, while the content of other analytes proportionally decreases with the increase of TiO_2 content.

Table 2
Calculated L_c and E_g values.

Sample	L_c [nm]	E_g [eV]	Sample	L_c [nm]	E_g [eV]
TiO_2(1)	6	3.11	TiO_2(6)	15	3.11
KATI12	–	3.25	KATI62	17	3.21
KATI14	6	3.22	KATI64	18	3.21
KATI16	7	3.17	KATI66	19	3.17

XRPD patterns of the K sample and the KATI composites dried at 105 °C is shown in Fig. 2. Quartz (Q; PDF number 85-0798) and muscovite (M; PDF number 7-0042) represent typical mineral admixtures accompanying pure KLT (PDF number 75-1593) in K. The presence of these admixtures is also in agreement with the chemical composition of the original K sample. The ideal molar ratio of SiO_2/Al_2O_3 in chemically pure KLT is 2. However, chemical analysis of the K sample revealed the molar ratio value 2.8 (see Table 1). The difference is caused by the mineral admixture. In the composites, the increase of TiO_2 (PDF number 86-1157) content led to the decrease of the KLT, M and Q fractions and consequently to the decrease of intensity for KLT, M and Q peaks. The segments of the region of 27–32° 2θ (CoK_α), where the anatase peak (1 0 1) occurs, is shown in Fig. 3. Only one broad anatase peak (1 0 1) is evident in the diffraction pattern of the pure TiO_2(1) powder sample, prepared by the same procedure as all the composites.

The diffraction patterns of samples calcined 2 h at 600 °C are presented in Fig. 4. After the calcination of the K sample (calcined kaolin is denoted as K6), diffraction peaks belonging to KLT almost disappear. During the KLT heating at the temperatures higher than approx. 470 °C, the K starts to loose its interlayer water what is generally described as dehydroxylation of the K structure [33], in fact the real temperature of onset of dehydroxylation is dependent on many factors. Release of the interlayer water from KLT is evidenced by the disappearing of its (0 0 1) basal diffraction peak. This process leads to formation of new amorphous phase called metakaolinite (MKLT) [34]. The low intensity (0 0 1) and (0 0 2) diffraction peaks of KLT observed for sample K6 indicate the incomplete KLT dehydroxylation. Therefore, it can be assumed that the rest of the original layered KLT structure still remains in the sample K6. The presence of the (1 0 1) anatase diffraction peak is clearly observable for all calcined composites. The presence of this peak is caused by the increase of size of the anatase crystallites during the calcination process. Lowering the intensity of quartz and muscovite peaks is caused by the decrease of fraction of these admixtures with increasing amount of TiO_2. The segments of the region of 27–32° 2θ (CoK_α), where the anatase peak (1 0 1) occurs, for the calcined samples is shown if Fig. 3. The anatase crystallite size for all of the KATI nanocomposites as well as the samples TiO_2(1) and TiO_2(6) was calculated according to the (101) anatase diffraction peak using Scherrer formula [35] and the values are shown in Table 2 (lanthanum hexaboride (LaB_6) was used as a standard). For pure TiO_2 as well as composites, it is evident that the anatase crystallite size grows after the calcination. The increasing amount of TiO_2 in composites does not significantly affect the anatase crystallite size for given heat treatment as is evident from the data in Table 2. The anatase crystallite size of pure TiO_2(6) is even smaller than those calculated for the calcined KATI6*X* composites.

Diffraction patterns of calcined samples in Fig. 3 show that in case of the K6 sample there is still the weak (0 0 1) basal reflection of KLT. This peak is missing in the diffraction patterns of the KATI composites calcined at 600 °C. That means the treatment with

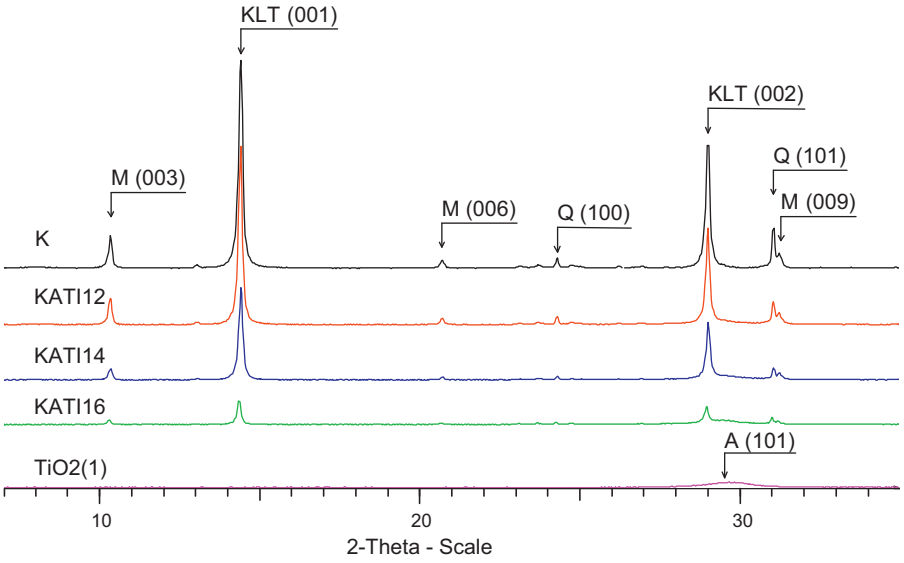

Fig. 2. XRPD pattern of samples dried at 105 °C. KLT, kaolinite; Q, quartz; M, muscovite; A, anatase.

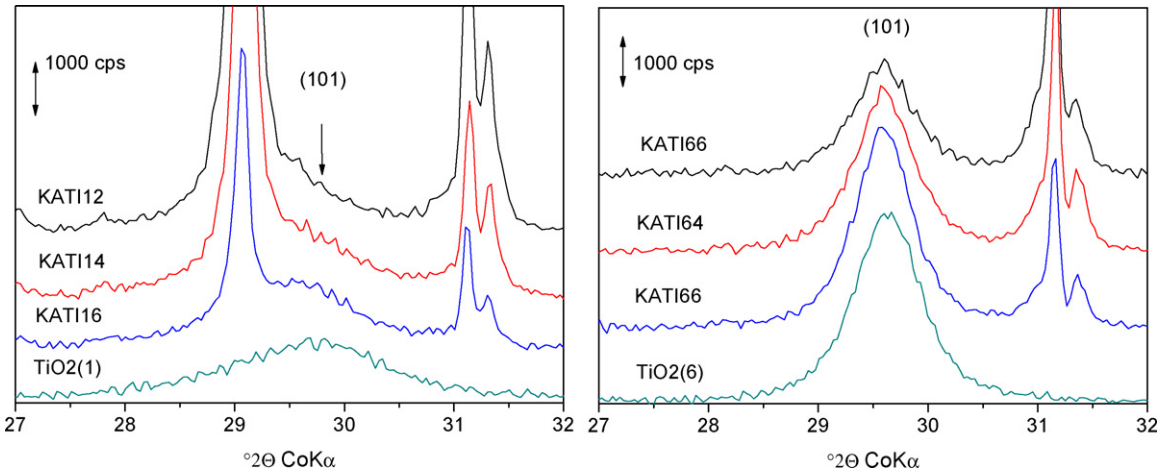

Fig. 3. The segments of diffraction patterns showing the region of (1 0 1) anatase and (0 0 1) kaolinite diffraction peaks for the dried (left) and calcined (right) samples.

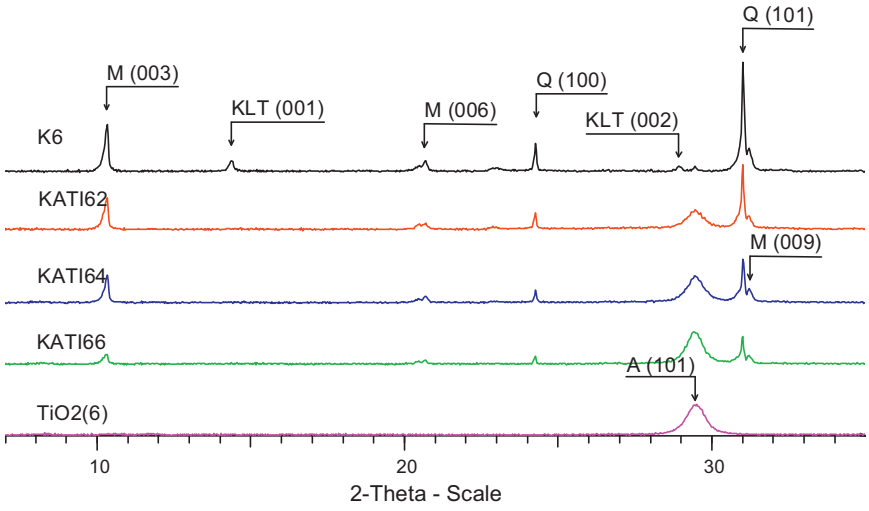

Fig. 4. X-ray powder diffraction pattern of samples calcined at 600 °C. KLT, kaolinite; Q, quartz; M, muscovite; A, anatase.

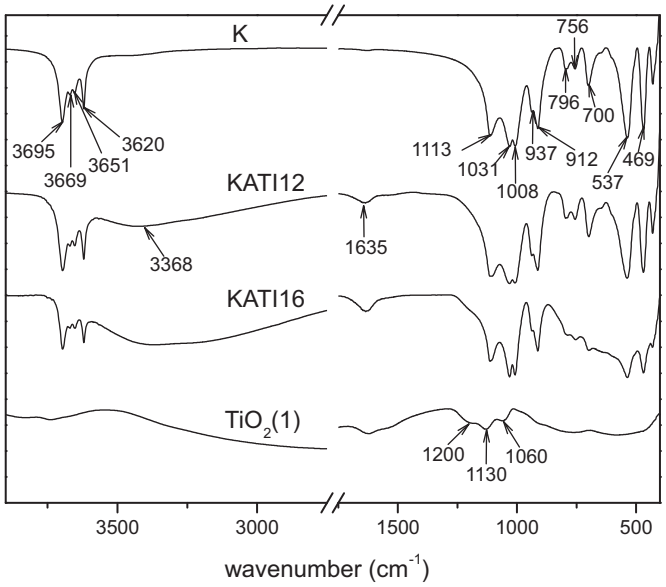

Fig. 5. IR spectra of non-calcined samples.

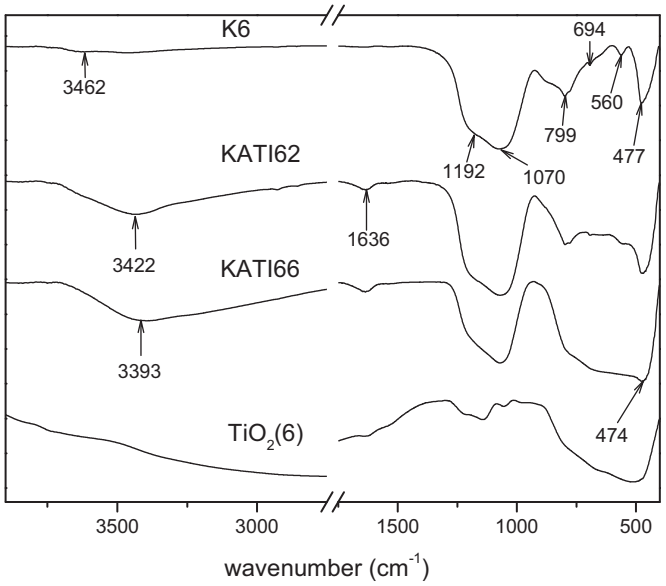

Fig. 6. IR spectra of samples calcined 2 h at 600 °C.

$TiOSO_4$ accelerated the phase transition of KLT → MKLT as a result of the chemical attack by sulfuric acid, which leads to the formation of the structural defects in the KLT layers, especially on the particle edges [36].

3.2. Optical properties of the prepared composites

Mid-infrared spectra of raw K, $TiO_2(1)$ and the KATI1*X* composites are shown in Fig. 5, and the IR spectra of samples calcined at 600 °C in Fig. 6. Peak maxima observed for the K sample before calcination (Fig. 4) corresponds to those wavelength values reported for pure KLT [37]. Bands with maxima at 3695, 3669, 3651, 3620 and 937, 912 cm^{-1} correspond to vibrations of inner and outer Al–OH bonds, bands at 1113, 1031, 1008, 796 and 469 cm^{-1} belong to vibrations of Si–O bonds, and bands at 756, 700, 537 cm^{-1} belong to vibrations of Si–O–$Al^{(IV)}$.

The profile and position of maxima observed at the IR spectra of the KATI12 sample are very similar to IR spectra registered for the raw K sample (Fig. 5) due to the low content of TiO_2. The band at 950 cm^{-1} attributed to Si–O–Ti antisymmetric stretching vibration [38] was not observed at the spectra of the KATI1X sample as well as KATI6X (at both *X* = 1 or 6), probably due to a small number of these bonds in prepared composites. Both broad band at approx. 3400 cm^{-1} and band with maximum at 1635 cm^{-1} observed at dried as well as calcined composites belong to vibration of O–H bond in adsorbed water. The broad bands at 1200, 1130 and 1060 cm^{-1} observed at the IR spectrum of $TiO_2(1)$ belong to bending vibration of Ti–O–H in the anatase phase [39].

In case of the calcined samples (see Fig. 6) the disappearance of bands in region 3700–3200 cm^{-1} belonging to O–H bonds observed in the K6 sample (Fig. 6) is clearly evident. This is the typical manifestation of a structure dehydroxylation and KLT → MKLT transformation [40]. Moreover, the change of band structure in the region 1250–400 cm^{-1} is the consequence of KLT → MKLT transformation leading to a change of Al^{3+} coordination from the octahedral in KLT to the tetrahedral in MKLT. Broad bands with maxima

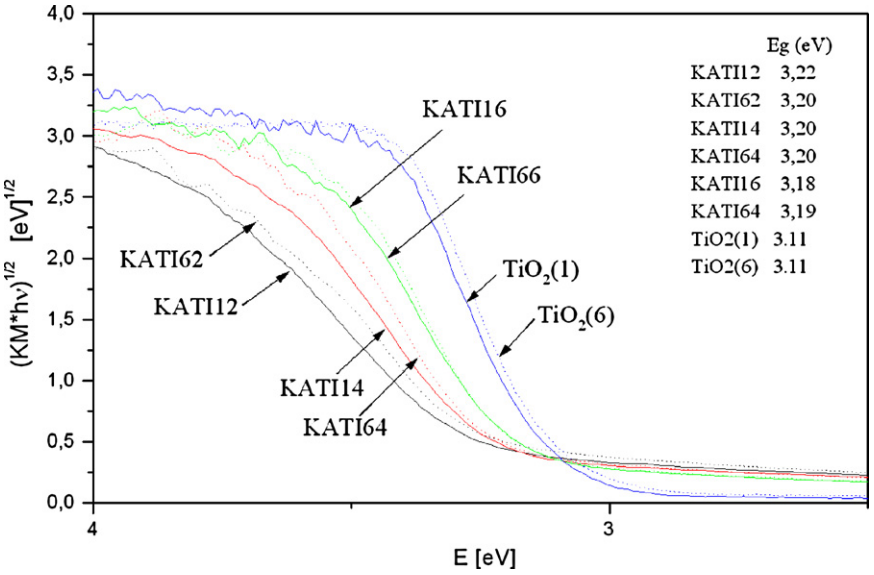

Fig. 7. UV–VIS diffuse reflectance spectra of the samples $TiO_2(1)$, $TiO_2(6)$, KATI12, KATI14, KATI16, KATI62, KATI64 and KATI66.

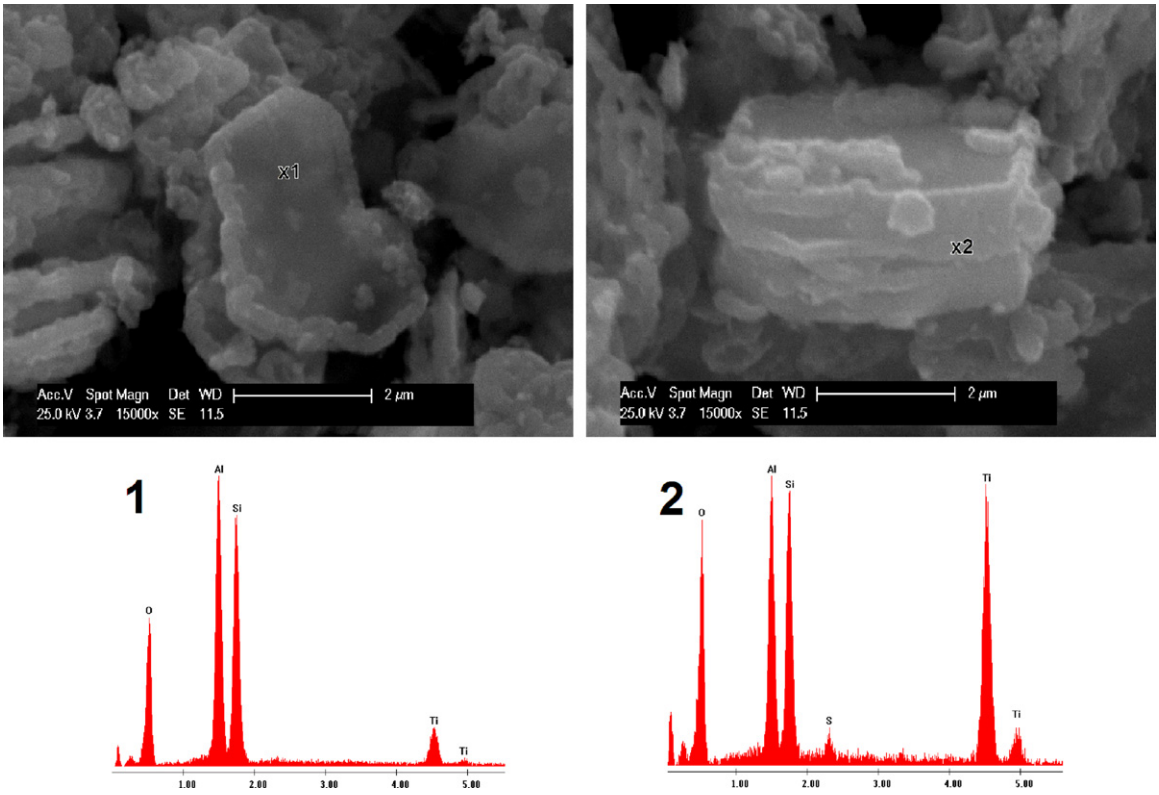

Fig. 8. SEM micrographs of KATI66 particles shows TiO_2 nanoparticles deposited mainly on KLT edges. This observation is confirmed by EDS.

at 1070 and 1192 cm^{-1} are attributed to the amorphous SiO_2 [37].

The reflectance spectra registered for composites KATI and pure TiO_2 in UV–VIS region were transformed to Kubelka–Munk coordinates (KM) and then expressed using Tauc plot [41] (Fig. 7) which shows the relation $(KM \times h\nu)^{1/2} = f(h\nu)$. For evaluation of the band gap (E_g) values, the method introduced by Kočí et al. [42] was adopted, whereas the calculated values are shown in Table 2 together with calculated values of L_c. The E_g values obtained for $TiO_2(1)$ and $TiO_2(6)$ samples reach the same value 3.11 eV. The values of band gap calculated for composites KATI are influenced by the TiO_2 content. Shift of the E_g values towards lower energies (red shift) is caused by the presence of larger TiO_2 particles which originate in the mixtures containing higher amount of $TiOSO_4$, the anatase crystallite size dependency on the amount of $TiOSO_4$ was also approved by X-ray diffraction method (see Table 2). Calcination of the composites also caused red shift of the E_g values which is again typical manifestation of the growing of the anatase crystallite size. The discrepancy in the relation between anatase crystallite size and the E_g values calculated for pure TiO_2 (lower anatase crystallite size but also lower E_g values) and composites (higher anatase crystallite size and higher E_g values) – see Table 2, is probably due to the synergistic effect of the KLT matrix and TiO_2 particles. With respect to this fact, it is necessary to bring the composites as a new material with given properties, which cannot be easily obtained by additive mechanism of the properties of the pure anatase and the pure KLT.

3.3. Study of composite particles morphology and texture parameters

Direct observation of TiO_2 particles anchored on the KLT surface was performed using SEM. The SEM micrographs showing the KATI66 particle morphology is pictured in Fig. 8. Both images show that TiO_2 particles are deposited mainly on the KLT edges. This visual observation was confirmed by EDS (see Fig. 8). TiO_2 nanoparticles start to grow on the edges and gradually form a border of the plate-like KLT particles. Similar observation has been published by Matějka et al. [29] for growing of CdS particles on the vermiculite edges. The effort of several authors was to prepare the photocatalytic nanoparticles in the 2:1 phyllosilicates interlayer space [43,30,44]. But evidently for the photocatalytic reactions the most efficient TiO_2 nanoparticles are those which are in direct contact with pollutant. This requirement is fulfilled by the particles anchored on the surface of the phyllosilicate matrix.

Table 3
The specific surface area of kaolinite and prepared composites.

Sample	SSA [m^2/g]	Sample	SSA [m^2/g]
K	9.5	K6	8.7
KATI12	59.6	KATI62	23.7
KATI14	67.1	KATI64	32.0
KATI16	64.8	KATI66	38.6

SSA of studied samples is shown in Table 3. SSA value measured for the K6 sample slightly decreased in comparison with the original K. The influence of calcination temperature of the selected kaolines on their SSA values shows, for example, Bich et al. [45]. The SSA values significantly increase at the KATI composites (Table 3). These values increase with the TiO_2 content up to 40 wt.% of TiO_2, further increase of TiO_2 content lead to the decrease of the SSA values. Growing of the SSA values with TiO_2 content is related to the origination of new TiO_2 surfaces and can be also associated with chemical activation of the KLT surface due to the chemical attack by sulfuric acid, which is main component of the $TiOSO_4$ colloid suspension [46]. Increase of SSA in dependence on the TiO_2 amount was previously observed by Kun et al. [43] for montmorillonite/TiO_2 composites.

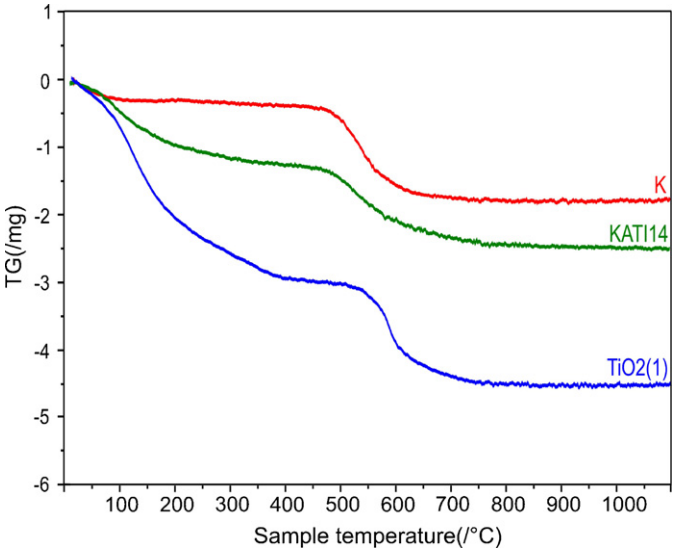

Fig. 9. Results of thermogravimetric measurements for samples K, KATI14 and $TiO_2(1)$.

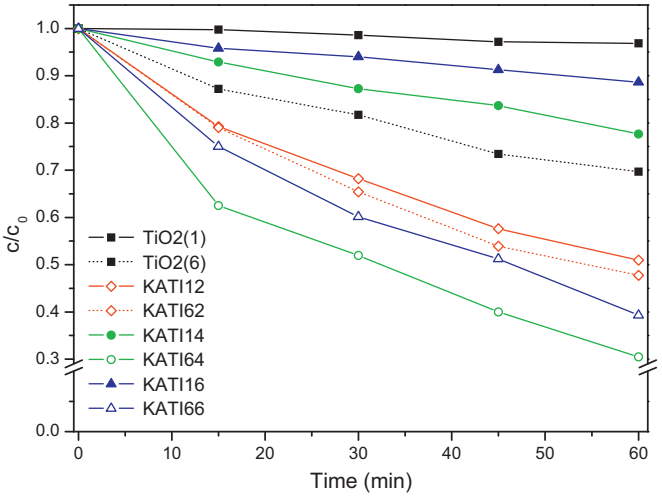

Fig. 10. Time dependency of acid orange 7 relative concentration for pure TiO_2 and composites dried at 105 °C ($TiO_2(1)$, KATI12, KATI14, KATI16) and calcined at 600 °C ($TiO_2(6)$, KATI62, KATI64, KATI66).

3.4. Study of the weight loss of samples during their heating

The weight loss of the samples K, KATI14 and $TiO_2(1)$ is pictured in Fig. 9. The weight loss of pure K in the temperature interval approx. 20–470 °C is not so obvious in comparison to pure $TiO_2(1)$ and composite KATI14. Changes in this temperature region are connected to loosing of water bonded on the TiO_2 surface. The higher the TiO_2 content, the higher the weight loss. The significant weight loss evident for sample K in the region 470–600 °C is connected with dehydroxylation of KLT structure what results in MKLT formation. MKLT having latent hydraulic properties is widely used in industry of building materials [47]. The on-set temperature of the KLT dehydroxylation is influenced by many factors and for KLT used at this work was determined as 464 °C. The sample KATI14 starts to lose weight continuously from the lowest testing temperature. The decrease in weight of $TiO_2(1)$ in region characteristic for KLT dehydroxylation cannot be connected to this phenomenon and is result of loosing of water absorbed on TiO_2 surface as well as to loosing of sulfur.

Sulfur content in $TiO_2(1)$ sample measured by combustion method and recalculated to SO_3 content is 8.17 wt.%, while sample $TiO_2(6)$ contain only 0.065 wt.%. The decrease in weight of KATI14 in region approx. 460–700 °C is given by the superposition of peaks originating from (a) dehydroxylation of KLT, (b) loosing water fixed on the TiO_2 surface and (c) loosing of sulfur, which is typical admixture of TiO_2 prepared by sulfate process.

3.5. Determination of photodegradation activity of prepared composites

Time dependency of the photodegradation activity of the prepared samples against AO7 is pictured in Fig. 10. $TiO_2(1)$ sample shows the lowest extent of photodegradation of AO7, only 10% after 1 h long UV irradiation. This value increased at sample $TiO_2(6)$ to reach approx. 30%. The second lowest photodegradation activity shows composite KATI16 which also significantly increased after calcination (KATI66) when reached almost 60%. Generally, the photodegradation activity for all samples increased after calcination at 600 °C. For samples dried at 105 °C we can conclude that the photodegradation activity decreases with increasing TiO_2 content. However in the case of calcined samples the highest photoactivity has been observed for KATI64 with medium TiO_2 content and the lowest activity was observed for sample KATI16. Similar results were observed Chong et al. [32]. Their KLT/TiO_2 composite prepared by the sol–gel method exhibit higher photodegradation activity in comparison to bare TiO_2 prepared in the absence of KLT by the same way as KLT/TiO_2 composite. Comparing all the curves in Fig. 10 we can also see that the calcination has a different effects for samples with a different TiO_2 contents. These findings lead to the conclusion that the photodegradation activity is a result of the interplay of many factors like TiO_2 content, the value of specific surface area, calcinations' conditions, presence of sulfur and its effect on the KLT structure, etc. In this study the composite KATI64 exhibits the best photoactive properties.

3.6. Study of the structure and adhesion forces using molecular modeling

Molecular modeling with an empirical force field as implemented in *MS* has been used to study (a) the structure of the KATI nanocomposite and (b) the adhesion forces between TiO_2 nanoparticles and the KLT matrix in order to predict structure and to evaluate the stability of composites.

To obtain the model of reasonable size, the structure of the "real" KLT $(Al_{7.8}Fe^{3+}{}_{0.16}K_{0.04})(Si_8)O_{20}(OH)_{16}$ was approximated by $(Al_8)(Si_8)O_{20}(OH)_{16}$ and the model KLT was built as a non-periodic superstructure containing six layers (see Fig. 11) with the total formula of $(Al_{1254})(Si_{1296})O_{3156}(OH)_{2640}$. This idealized model without tetrahedral cationic substitutions has the total layer charge of −6 el. coming fully from the non-stoichiometry on the edges. The layer charge was compensated by the anchored TiO_2 nanoparticle. The size of the KLT matrix is 5.1 nm × 4.4 nm; thickness ~4.1 nm. Interlayer distance (basal spacing) corresponding to the real structure 0.74 nm [48] has been used in this model.

Four types of TiO_2 nanoparticles (anatase structure) with crystallographic orientations (0 0 1) and (1 0 0) and with the charge +6 el. have been prepared in two sizes, $Ti_{39}O_{75}$ and $Ti_{78}O_{153}$, respectively. The similarity of nanoparticles with different crystallographic orientations for possible comparison was warranted by the fulfillment of the two following conditions: (a) the same number of atoms in whole nanoparticle and (b) the same number of atoms in the plane adjacent to the KLT layer (24 atoms in the case of $Ti_{39}O_{75}$ and 48 atoms in the case of $Ti_{78}O_{153}$). Because the distribution of atoms in various *h k l* planes is not the same, condition (b) constrained each nanoparticle to have a different lengths of basal

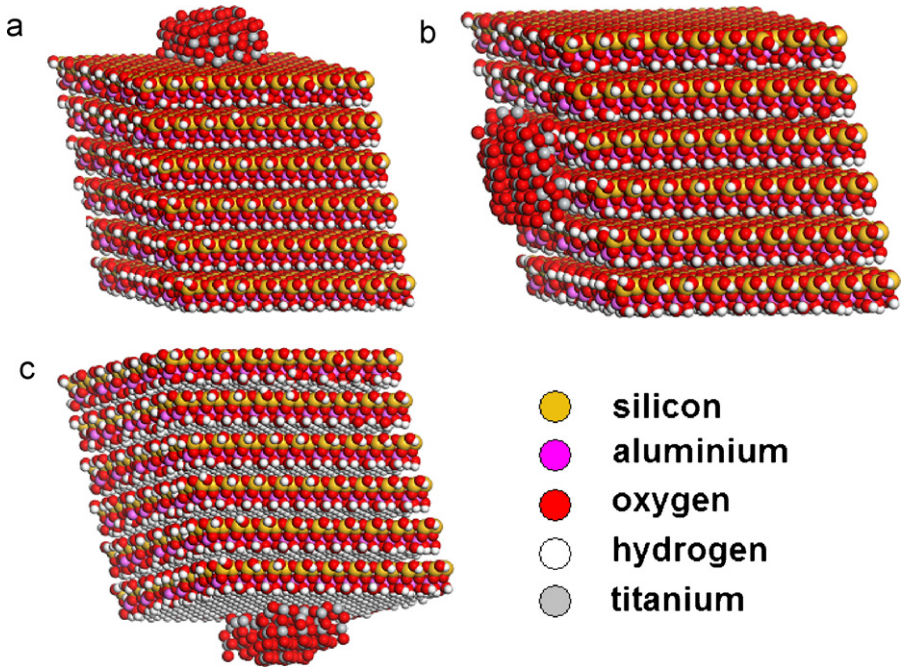

Fig. 11. Optimized models of TiO_2 (0 0 1) nanoparticle (231 atoms) anchored on (a) tetrahedral surface, (b) edge and (c) octahedral surface of the KLT matrix.

Table 4
The values of the adhesion energy calculated for TiO_2 nanoparticles anchored on various faces of KLT matrix. Value *n* indicates the number of atoms in the nanoparticle.

n	Location	Adhesion energy [kcal]	
		TiO_2 (0 0 1)	TiO_2 (1 0 0)
114	SiO surface	2085	2242
	Edge	4464	3948
	OH surface	2693	1978
231	SiO surface	4697	4657
	Edge	8718	8345
	OH surface	6148	5632

diagonal (i.e., size of TiO_2 nanoparticles in the diagonal direction of basal planes). Hence for the crystallographic orientations (0 0 1) and (1 0 0), the lengths of basal diagonal are (in case of $Ti_{39}O_{75}$) 1.47 nm and 1.52 nm, in the case of $Ti_{78}O_{153}$ 2.27 nm and 2.51 nm. Initial models have been prepared by anchoring each nanoparticle to one of the three possible types of KLT matrix–tetrahedral surface (basal SiO surface; see Fig. 11a), edge (see Fig. 11b) and octahedral surface (basal OH surface; see Fig. 11c). QEq (charge equilibration) method in *MS* has been used to calculate the atomic charges [49]. The interaction between the TiO_2 nanoparticles and the silicate substrate was quantified using the adhesion energy

$$E_{ad} = (E_{tot,TiO_2} + E_{tot,KLT}) - E_{tot} \quad (1)$$

where E_{tot} is the total energy of the nanocomposite (i.e., the TiO_2 nanoparticle anchored on the KLT substrate). E_{tot,TiO_2} is the total energy of the TiO_2 nanoparticle and $E_{tot,KLT}$ is the total energy of the KLT substrate. These energies are expressed in the unit [kcal] and have been calculated using the UFF [50] in *MS Forcite module*. In our previous works the UFF proved to be the suitable force field for the modeling of layer silicate/nanoparticle nanocomposites [29,51].

Calculated adhesion energies are listed in Table 4. The adhesion energies were computed using Eq. (1). It is evident that models containing the TiO_2 nanoparticle anchored on a KLT edge exhibit the best (i.e., the highest) adhesion energies for both crystallographic faces of TiO_2: (1 0 0) and (0 0 1). The face (0 0 1) is slightly preferred which allows us to consider this arrangement as the most stable. Table 4 also shows the higher "unwillingness" of TiO_2 nanoparticles to grow on the tetrahedral and octahedral surface. This result is in good agreement with the observations by the SEM analysis of the KATI nanocomposite (see Fig. 8), where we can see TiO_2 on the KLT edges.

4. Conclusion

The photoactive KATI composites were successfully prepared using $TiOSO_4$ as an inexpensive precursor of TiO_2, which is also widely accessible intermediate from the sulfate process of TiO_2 pigment manufacturing. On contrary to pure TiO_2 nanoparticles, this composite is based on the fixed TiO_2 nanoparticles on the significantly bigger particles of aluminosilicate matrix. This technology minimizes environmental risks of TiO_2 nanoparticles, and makes manipulation with this nanocomposite safer. It was found by molecular modeling, that TiO_2 particles grow preferably on the edges of KLT particles and do not form the compact layer fully covering the surface of KLT particles. This result was verified by SEM observations, confirming the modeling as a valuable tool for structure and stability prediction in the case of these composites. The photodegradation activity of TiO_2 and dehydroxylation phenomenon of KLT which leads to MKLT formation is preserved with KATI composites. It is important fact as the MKLT is valuable material with latent hydraulic properties. That means this composite brings two benefits as a component of building materials: latent hydraulic properties and photocatalytic activity.

Calcined KATI composites were also found to show higher photodegradation activity in comparison with dried composites. This phenomenon is not related to the increase of SSA, which, after calcination, decreases. The most probable effect is the decrease of sulfur content which predominantly occurs as free sulfuric acid absorbed on the TiO_2 surface. The fact that KLT transforms after thermal treatment to MKLT (a widely studied material showing latent hydraulic properties) allows the KATI composite to find wide application in the building industry.

Acknowledgements

The research has been funded by the Czech Ministry of Industry and Trade (project FT-TA4/025), by the Grant Agency of Czech Republic (project GA205/08/0869) and by the projects of Ministry of Education of Czech Republic (projects SP/2010140 and SP/201046). The authors would like to thank Daniel Casten for language corrections.

References

[1] U. Diebold, The surface science of titanium dioxide, Surf. Sci. Rep. 48 (2003) 53–229.
[2] O. Carp, C.L. Huisman, A. Reller, Photoinduced reactivity of titanium dioxide, Prog. Solid State Chem. 32 (2004) 33–177.
[3] C. Xiabo, S.S. Mao, Synthesis of titanium dioxide (TiO_2) nanomaterials, J. Nanosci. Nanotechnol. 6 (2006) 906–925.
[4] M. Asiltürk, F. Sayılkan, S. Erdemoğlu, M. Akarsu, H. Sayılkan, M. Erdemoğlu, E. Arpaç, Characterization of the hydrothermally synthesized nano-TiO_2 crystallite and the photocatalytic degradation of rhodamine B, J. Hazard. Mater. 129 (2006) 164–170.
[5] J. Klongdee, W. Petchkroh, K. Phuempoonsathaporn, P. Praserthdam, A.S. Vangnai, V. Pavarajarn, Activity of nanosized titania synthesized from thermal decomposition of titanium (IV) *n*-butoxide for the photocatalytic degradation of diuron, Sci. Technol. Adv. Mater. 6 (2005) 290–295.
[6] D.V. Bavykin, V.P. Dubovitskaza, A.V. Vorontsov, V.N. Parmon, Effect of $TiOSO_4$ hydrothermal hydrolysis conditions on TiO_2 morphology and gas-phase oxidative activity, Res. Chem. Intermed. 33 (2007) 449–464.
[7] Q. Yhang, L. Gao, Preparation of nanocrystalline TiO_2 powders for photocatalytic oxidation of phenol, Res. Chem. Intermed. 35 (2009) 281–286.
[8] F. Han, V.S. Rao Kambala, M. Srinivasan, D. Rajarathnam, R. Naidu, Tailored titanium dioxide photocatalysts for the degradation of organic dyes in wastewater treatment, Appl. Catal. A 359 (2009) 25–40.
[9] N. Kashif, F. Ouyang, Parameters effect on heterogeneous photocatalysed degradation of phenol in aqueous dispersion of TiO_2, J. Environ. Sci. 21 (2009) 527–533.
[10] M.V. Phanikrishna Sharma, G. Sadanandam, A. Ratnamala, V.D. Kumari, M. Subrahmanyam, An efficient and novel porous nanosilica supported TiO_2 photocatalyst for pesticide degradation using solar light, J. Hazard. Mater. 171 (2009) 626–633.
[11] Z. Wu, H. Wang, Y. Liu, Z. Gu, Photocatalytic oxidation of nitric oxide with immobilized titanium dioxide films synthesized by hydrothermal method, J. Hazard. Mater. 151 (2008) 17–25.
[12] G. Colón, M. Maicu, M.C. Hidalgo, J.A. Navío, A. Kubacka, M. Fernández-García, Gas phase photocatalytic oxidation of toluene using highly active Pt doped TiO_2, J. Mol. Catal. A: Chem. 320 (2010) 14–18.
[13] T.X. Liu, F.B. Li, X.Z. Li, TiO_2 hydrosols with high activity for photocatalytic degradation of formaldehyde in a gaseous phase, J. Hazard. Mater. 152 (2008) 347–355.
[14] C. Chawengkijwanich, Y. Hayata, Development of TiO_2 powder-coated food packaging film and its ability to inactivate *Escherichia coli* in vitro and in actual tests, Int. J. Food Microbiol. 123 (2008) 288–292.
[15] D.B. Warheit, R.A. Hoke, C. Finlay, E. Maria Donner, K.L. Reed, C.M. Sayes, Development of a base set of toxicity tests using ultrafine TiO_2 particles as a component of nanoparticle risk management, Toxicol. Lett. 171 (2007) 99–110.
[16] S.Q. Li, R.R. Zhu, H. Zhu, M. Xue, X.Y. Sun, S.D. Yao, S.L. Wang, Nanotoxicity of TiO_2 nanoparticles to erythrocyte in vitro, Food Chem. Toxicol. 46 (2008) 3626–3631.
[17] R. Kaegi, A. Ulrich, B. Sinnet, R. Vonbank, A. Wichser, S. Zuleeg, H. Simmler, S. Brunner, H. Vonmont, M. Burkhardt, M. Boller, Synthetic TiO_2 nanoparticle emission from exterior facades into the aquatic environment, Environ. Pollut. 156 (2008) 233–239.
[18] L. Reijnders, The release of TiO_2 and SiO_2 nanoparticles from nanocomposites, Polym. Degrad. Stab. 94 (2009) 873–876.
[19] A. Nikolopoulou, D. Papoulis, S. Komarneni, P. Tsolis-Katagas, D. Panagiotaras, G.H. Kacandes, P. Zhang, S. Yin, T. Sato, Solvothermal preparation of TiO_2/saponite nanocomposites and photocatalytic activity, Appl. Clay Sci. 46 (2009) 363–368.
[20] S. Ouidri, H. Khalaf, Synthesis of benzaldehyde from toluene by a photocatalytic oxidation using TiO_2-pillared clays, J. Photochem. Photobiol. A 207 (2009) 268–273.
[21] H. Chorfi, G. Zayani, M. Saadoun, L. Bousselmi, B. Bessaïs, Understanding the solar photo-catalytic activity of TiO_2–ITO nanocomposite deposited on low cost substrates, Appl. Surf. Sci. 256 (2010) 2170–2175.
[22] A. Kafizas, S. Kellici, J.A. Darr, I.P. Parkin, Titanium dioxide and composite metal/metal oxide titania thin films on glass: a comparative study of photocatalytic activity, J. Photochem. Photobiol. A 204 (2009) 183–190.
[23] T. Watanabe, A. Nakajima, R. Wang, M. Minabe, S. Koizumi, A. Fujishima, K. Hashimoto, Photocatalytic activity and photoinduced hydrophilicity of titanium dioxide coated glass, Thin Solid Films 351 (1999) 260–263.
[24] M. Bellardita, M. Addamo, A. Di Paola, G. Marcì, L. Palmisano, L. Cassar, M. Borsa, Photocatalytic activity of TiO_2/SiO_2 systems, J. Hazard. Mater. 174 (2010) 707–713.
[25] R.B. Zhang, Photodegradation of toluene using silica-embedded titania, J. Non-Cryst. Solids 351 (2005) 2129–2132.
[26] M.G. da Fonseca, M.M. de Oliveira, L.N.H. Arakaki, Removal of cadmium, zinc, manganese and chromium cations from aqueous solutions by a clay mineral, J. Hazard. Mater. 137 (2006) 288–292.
[27] L. Koröosi, J. Németh, I. Dékány, Structural and photooxidation properties of SnO_2/layer silicate nanocomposites, Appl. Clay Sci. 27 (2004) 29–40.
[28] T. Szabó, J. Németh, I. Dékány, Zinc oxide nanoparticles incorporated in ultrathin layer silicate films and their photocatalytic properties, Colloids Surf. A: Physicochem. Eng. Aspects 230 (2003) 23–35.
[29] V. Matějka, M. Šupová, V. Klemm, D. Rafaja, M. Valášková, J. Tokarský, J. Lešková, E. Plevová, Vermiculite interlayer as a reactor for CdS ultrafine particles preparation, Micropor. Mesopor. Mater. 129 (2010) 118–125.
[30] Y. Kameshima, Y. Tamura, A. Nakajima, K. Okada, Preparation and properties of TiO_2/montmorillonite composites, Appl. Clay Sci. 45 (2009) 20–23.
[31] L.C.R. Machado, C.B. Torchia, R.M. Lago, Floating photocatalysts based on TiO_2 supported on high surface area exfoliated vermiculite for water decontamination, Catal. Commun. 7 (2006) 538–541.
[32] M.N. Chong, V. Vimonses, S. Lei, B. Jin, C. Chow, C. Saint, Synthesis and characterisation of novel titania impregnated kaolinite nano-photocatalyst, Micropor. Mesopor. Mater. 117 (2009) 233–242.
[33] R. Fernandez, F. Martirena, K.L. Scrivener, The origin of the pozzolanic activity of calcined clay minerals: a comparison between kaolinite, illite and montmorillonite, Cem. Concr. Res. 41 (2011) 113–122.
[34] A. Shvarzman, K. Kovler, G.S. Grader, G.E. Shter, The effect of dehydroxylation/amorphization degree on pozzolanic activity of kaolinite, Cem. Concr. Res. 3 (2003) 405–416.
[35] P. Scherrer, Estimation of size and internal structure of colloidal particles by means of Röntgen rays, Nachr. Ges. Wiss. Gottingen (1918).
[36] A.K. Panda, B.G. Mishra, D.K. Mishra, R.K. Singh, Effect of sulphuric acid treatment on the physicochemical characteristics of Kaolin clay, Colloids Surf. A 363 (2010) 98–104.
[37] H. Beutelspacher, H.W. van der Marel, Atlas of Infrared Spectroscopy of Clay Minerals and Their Admixtures, Elsevier, Amsterdam, 1976, ISBN 0-444-41187-9.
[38] X. Gao, I.E. Wachs, Titania–silica as catalysts: molecular structural characteristics and physico-chemical properties, Catal. Today 51 (1999) 233–254.
[39] T. Bezrodna, G. Puchkovska, V. Shymanovska, J. Baran, H. Ratajczak, IR-analysis of H-bonded H_2O on the pure TiO_2 surface, J. Mol. Struct. 700 (2004) 175–181.
[40] G. Kakali, T. Perraki, S. Tsivilis, E. Badogiannis, Thermal treatment of kaolin: the effect of mineralogy on the pozzolanic activity, Appl. Clay Sci. 20 (2001) 73–80.
[41] J. Tauc, R. Grigorovici, A. Vancu, Optical properties and electronic structure of amorphous germanium, Phys. Status Solidi 15 (1966) 627–637.
[42] K. Kočí, L. Obalová, L. Matějová, D. Plachá, Z. Lacný, J. Jirkovský, O. Šolcová, Effect of TiO_2 particle size on the photocatalytic reduction of CO_2, Appl. Catal. B. 89 (2009) 494–502.
[43] R. Kun, K. Mogyorósi, I. Dékány, Synthesis and structural and photocatalytic properties of TiO_2/montmorillonite nanocomposites, Appl. Clay Sci. 32 (2006) 99–110.
[44] J. Liu, X. Li, S. Zuo, Y. Yu, Preparation and photocatalytic activity of silver and TiO_2 nanoparticles/montmorillonite composites, Appl. Clay Sci. 37 (2007) 275–280.
[45] C. Bich, J. Ambroise, J. Péra, Influence of degree of dehydroxylation on the pozzolanic activity of metakaolin, Appl. Clay Sci. 44 (2009) 194–200.
[46] A.K. Panda, B.G. Mishra, D.K. Mishra, R.K. Singh, Effect of sulphuric acid treatment on the physicochemical characteristics of kaolin clay, Colloids Surf. A: Physicochem. Eng. Aspects 36 (2010) 98–104.
[47] R. Siddique, J. Klaus, Influence of metakaolin on the properties of mortar and concrete: a review, Appl. Clay Sci. 43 (2009) 392–400.
[48] R.B. Neder, M. Burghammer, T. Grasl, H. Schulz, A. Bram., S. Fiedler, Refinement of the kaolinite structure from single-crystal synchrotron data, Clays Clay Miner. 47 (1999) 487–494.
[49] A.K. Rappe, W.A. Goddard, Charge equilibration for molecular dynamics simulations, J. Phys. Chem. 95 (1991) 3358–3363.
[50] A.K. Rappe, C.J. Casewit, K.S. Colwell, W.A. Goddard, W.M. Skiff, UFF, a full periodic table force field for molecular mechanics and molecular dynamics simulations, J. Am. Chem. Soc. 114 (1992) 10024–10035.
[51] J. Tokarský, P. Čapková, D. Rafaja, V. Klemm, M. Valášková, J. Kukutschová, V. Tomášek, Adhesion of silver nanoparticles on the clay substrates; modeling and experiment, Appl. Surf. Sci. 256 (2010) 2841–2848.